STUDY ON LAND SURFACE TEMPERATURE CHARACTERISTICS OF HOT MUD ERUPTION IN EAST JAVA, INDONESIA

Luhur Bayuaji[1]**, Hiroshi Watanabe**[1]**, Hideyuki Tonooka**[2]**,**
Josaphat Tetuko Sri Sumantyo[1]**, and Hiroaki Kuze**[1]

Abstract. Hot mud has erupted in Sidoarjo, east Java, Indonesia since 29 May 2006. It started as natural gas exploration project and punctured a geological structure at a depth of 2.8 km, releasing unprecedented volume of hot mud volcano (5×104 m^3/day). By November 2006, it was estimated that hot mud had spread over $(2.89 \pm 0.10) \times 106$ m^2, swamping several villages with more than 10,000 people evacuated. In this research, by employing the advantage of spatial perspective of remote sensing imagery, the extent of hot mud spreading area and temperature distributions are derived from satellite images of the Advanced Spaceborne Thermal Emission and Reflection Radiometer (ASTER) sensor onboard the Terra satellite. The mud spreading area was calculated using three visible/near-infrared channels having a resolution of 15 m. Temperature distributions were calculated using the temperature/emissivity separation (TES) method on five thermal infrared channels with a resolution of 90 m. The standard and water vapor scaling (WVS) methods were applied in the atmospheric correction process prior to the TES process. The result showed that the mud continued spreading during five months after the eruption. After 3-5 months from the eruption, the estimated temperature was about 30-69°C in the mud spreading area. Also, estimations of the volume and weight of the hot mud were made on the basis of the visible of level 3A product of ASTER and ground survey data.

Keywords: *ASTER TIR, ASTER VNIR, Hot mud volcano, Temperature emissivity separation, Water vapor scaling method*

1. Introduction

Two days after a strong earthquake hit Yogyakarta, Central Java, a mud volcano mixed with stream of hot water erupted at 200 m away from Banjar Panji I hydrocarbon exploration well (Lapindo Brantas Inc.) in Sidoarjo, East Java, Indonesia on 29 May 2006 (Davies et al., 2006). In the hydrocarbon exploration well, the drilling had reached a depth of 2.8 km when the accident occurred. The drill string was stuck in the well, resulting in the catastrophic eruption of a geyser of mud and hot water with a flow rate of $(5-18) \times 104$ m3/day (Mazzini et al., 2007).

By November 2006, the mud had spread over 2.4×106 m^2, swamping nearby villages including schools, factories, roads, farms, paddy fields, and rail roads. In September 2006, more than 10,000 people in the region were affected by this calamity (Normile, 2006). Along with the mud eruption, some toxic gases and materials have been released to the environment. According to the investigation of United Nation Disaster Assessment and Coordination (UNDAC), however, the concentration of hydrogen sulfide and other toxic gases (H_2S, NO_2, CO, SO_2) are low. Concentrations of mercury and other metals in the mud were below safety standards (UNDAC, 2006).

[1] Center for Environmental Remote Sensing, Chiba University, 1-33 Yayoi-cho, Inage-ku, Chiba 263-8522, Japan.
[2] Department of Computer and Information Sciences, Ibaraki University, Ibaraki 316-8511, Japan.

Even if such pollution turns out to be non-hazardous, hot temperature itself can be threatening to the aquatic ecosystem. In fact, high volume of high-temperature mud has destroyed paddy fields and has turned houses and factories uninhabitable. It also will affect the ecosystem of the Porong River, a river next to the site (Figure 1). Vital infrastructures in the radius of spreading area, including main road, railways, a high-voltage electricity transmission line and a gas pipeline, which belongs to the National Oil and Gas Company (PERTAMINA) East Java, were buried under the site. On 22 November 2006, this gas pipeline exploded and killed 13 people on the spot. High temperature and heavy weight of hot mud were suspected as the main factor in this accident (Cyranoski, 2007).

In order to prevent the further spread of the mud area, the government immediately built artificial embankments (man-made dam) that surround the mud eruption site. Because of the high mud volume, however, the embankments collapsed repeatedly. This led to further actions such as constructing a larger, secondary embankment system (named a "pond system"), diverting the mud flow to the Porong River and constructing a canal for draining the mud into the sea. In November 2006, the diameter of the pond system was about 2 km, covering many areas such as villages, paddy fields, factories and many living infrastructures.

ASTER sensor, installed on Terra satellite, has ability to collect high spatial-resolution multispectral data in the wavelength range of 0.56-11.65 μm divided into three spectral ranges (Fujisada, 1994). ASTER data has been used to analyze various phenomena on the Earth surface such as flood (Tralli et al., 2005), glacier (Berthier et al., 2007; Paul et al., 2004), volcano activities (Pieri and Abrams, 2004; Ramsey and Dehn, 2004),

and urban thermal conditions (Pu et al., 2006). The present research will show the ability of ASTER to examine characteristics of mud eruption as part of Earth surface phenomena and application of ASTER data to such a disaster.

In an effort of evaluating this catastrophic event, this research examines hot-mud expansion size and temperature distribution in the hot-mud spreading area using remotely sensed data from visible and near infrared (VNIR) and longwave thermal infrared (TIR) channels of the ASTER sensor onboard the Terra satellite. The spatial expansion of the spreading area was retrieved using three VNIR channels, and the surface temperature of the relevant surface area was retrieved using five TIR channels. Other pieces of information such as the depth (embankment height) and weight of mud were also estimated by employing VNIR channels of ASTER data and the mud data obtained from the mud sample taken during a ground survey in November 2006. As a whole, this research exemplified the advantage of remote sensing, especially ASTER data, when applied to such a widely spread calamity. This study was organized as follow; section 2 is explaining about study site, data and methodology, including the standard and WVS atmospheric correction method. Section 3 is results and discussion section.

2. Methods
2.1. Study Site: Porong area

Porong district in Sidoarjo, East Java, Indonesia, is geographically located at 7°30´19"-7°33´46" S and 112°41´0"-112°44´1" E, about 900 km east of Jakarta and 14 km south of Surabaya (Figure 1(a)). The land surface elevation of Porong area is in a range of 0-25 m above sea level (ASL), but the mud eruption site in the range 1-5 m ASL. The bedrock type in this area is Holocene volcanic and the soil

structure type is gray alluvial. Annual average air temperature is 27°C with average humidity of 40-80%.

Annual average rainfall was 1,612 mm and 1,626 mm in the year 2005 and 2006, respectively (Public Work Department Website, 2008; Sidoarjo District Website, 2006; Surabaya Goverment Website, 2006): the rainfall rate increased during November until April. The district was divided into 19 villages including 8 villages that were swamped by hot mud. The study area, with a population of about 63000 (in March 2006), was covered not only by resident areas, paddy fields and factories but also by public infrastructures such as a highway, a railroad, city roads, a high-voltage distribution line, and a gas-pipe distribution line, as shown in Figure 1(a) (BAKOSURTANAL, 1997). The Banjar Panji I well, the center of hot mud eruption is marked as T1 and T2.

The ground data (pictures, surface temperatures, mud sample, and elevation data) were collected on 8 November 2006. Figure 1(b) shows the picture of the highway, the level of which was elevated by 5 m from its original level. The 15 m embankment has recently been built along the side of the highway to detain hot-mud flow. The presence of about 100 m high smoke in Figure 1(c) indicates the location of the eruption center. The smoke seen in the figure is due to hot and high pressure water flow from the Banjar Panji I well.
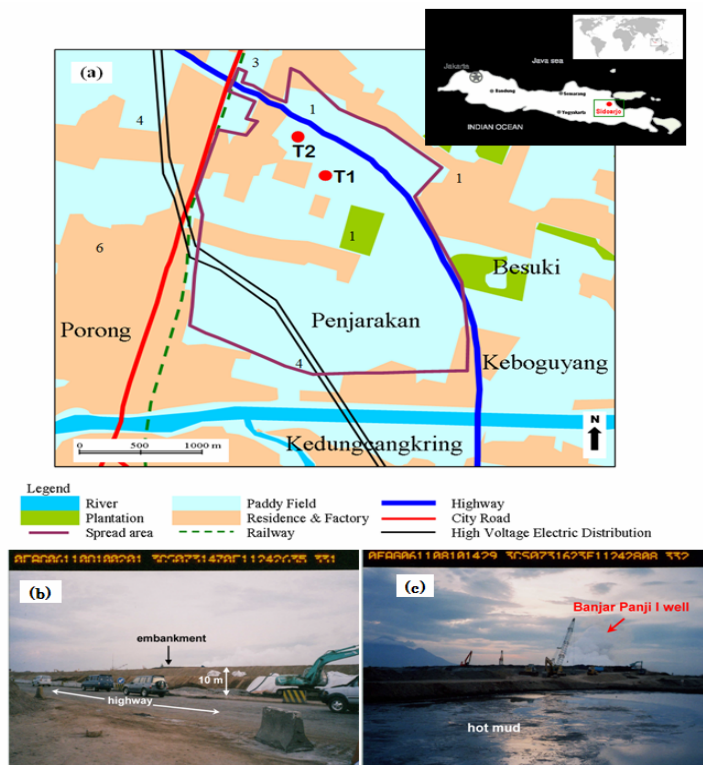

Figure 1. Study area: (a) study area map; T1 and T2 are the points of the erupted well; numbers 1-6 denote the above-sea-level surface height, (b) picture of the embankment constructed to prevent the further spread of the hot mud, and (c) appearance of hot mud nearby the Banjar Panji I well, the eruption point.

2.2. ASTER Data

The ASTER scenes were selected from ASTER Ground Data System on Earth Remote Sensing Data Analysis Center (ERSDAC) web site. The searching process for images from November 2005 until June 2008 resulted in 20 scenes, in which only 3 scenes were worth further processing since other images were found to be covered by cloud. In this study, we employed level-3A (L3A) product of ASTER images. First image (3 November 2005) was acquired seven months before the mud eruption (29 May 2006), and two images (3 September 2006 and 13 November 2006) 3 and 5 months after the eruption. The size of mud spreading area, mud volume and weight were analyzed from three VNIR channels (ch.1 through 3, covering a wavelength range of 0.52-0.86 μm). Image data from five TIR channels (ch.10 through channel 14, covering a wavelength range of 8-12 μm) were analyzed to obtain temperature information. The ground resolution of ASTER VNIR and TIR channels is 15 m and 90 m, respectively, with the maximum viewing angle of 11°. Full description of the ASTER sensor and its standard products were given in Abrams (2000).

2.3. Data Analysis

2.3.1. NDVI and Classification

Numerous studies have demonstrated that remote sensing is an effective tool for natural resource inventory/interpretation and environmental monitoring including land characterization. Especially, monitoring of land changes can be achieved using multi-temporal and multi-resolution data (Brack, 2007; McRoberts and Tomppo, 2007; Mezned et al., 2007; Miura et al., 2008; Muukkonen and Heiskanen, 2007).

The mud eruption site was previously a large crop and paddy field area with a small part of residence area. By monitoring the vegetation dynamics using the normalized difference vegetation index (NDVI) (Hussin and Atmopawiro, 2004; Tucker, 1979), dynamic changing of non-vegetation objects including mud can be detected. NDVI can be computed as (Paola and Schowengerdt, 1995):

$$NDVI = \frac{\rho_{NIR} - \rho_{RED}}{\rho_{NIR} + \rho_{RED}} \qquad (1)$$

where ρ_{RED} and ρ_{NIR} are the reflectivity at the red and near-infrared part of the spectrum (band 2 and band 3), respectively.

The maximum-likelihood classifier, one of the most common techniques in image classification, is used here to classify land characteristics and detect changes in land coverage. The maximum-likelihood classifier is a parametric classifier that relies on the second-order statistics of a Gaussian probability density function (pdf) that models each class. This method was often used as a reference for comparison of different classifiers, since in many cases the Gaussian pdf gives optimal result. The basic discriminant function for each class can be written (Paola and Schowengerdt, 1995) as:

$$g_{i(X)} = p((X)|w_i)p(w_i)$$

$$= \frac{p(w_i)}{(2\pi)^{n/2}|\Sigma_i|^{1/2}} e^{1(1/2)(X-U_i)^T \Sigma_i^{-1}(X-U_i)} \qquad (2)$$

where w_i is the image spectral classes, i is number of classes, $p(w_i)$ is probability that class w_i occur in the image, $p((X)|w_i)$ is the probability of a pixel from class w_i at the position X, n is the number of bands, X is the data vector, U_i is the mean vector of class i, e is Euler's number (e ≈ 2.718) and Σ_i is the covariance matrix of class i. The vectors

X and Ui, and the matrix Σ_i can be given as

$$X = \begin{bmatrix} x_i \\ x_i \\ \cdot \\ \cdot \\ \cdot \\ x_n \end{bmatrix}, \qquad U_i = \begin{bmatrix} \mu_{i1} \\ \mu_{i2} \\ \cdot \\ \cdot \\ \cdot \\ \mu_{in} \end{bmatrix}$$

$$\Sigma_i = \begin{bmatrix} \sigma_{i11} & \cdots & \sigma_{i1n} \\ \vdots & \ddots & \vdots \\ \sigma_{in1} & \cdots & \sigma_{inn} \end{bmatrix} \qquad (3)$$

The value in the mean vector, U_i, and the covariance matrix, Σ_i, are estimated from the training data by means of the following unbiased estimators:

$$\hat{\mu}_{ij} = \frac{1}{P_i} \sum_{l=1}^{P_i} x_{jl} \qquad j = 1, 2, \ldots, n. \qquad (4)$$

and

$$\hat{\sigma}_{ijk} = \frac{1}{P_i - 1} \sum_{d=1}^{P_i} \left(x_{jl} - \hat{\mu}_{ij} \right) \left(x_{kl} - \hat{\mu}_{ik} \right) \quad (j=1,2,\ldots,n; k=1,2,\ldots,n) \qquad (5)$$

where P_i is the number of pixel in the training area of class i. In order for the inverse of the covariance matrix to be calculated, P_i must be at least one greater than the number of image bands. By taking the natural log and discarding the constant π term, eq. (2) can be reduced to:

$$g_i(X) = \log_e p(w_i) - \frac{1}{2} \log_e |\Sigma_i| - \frac{1}{2} (X - U_i)^T \square \sum_i^{-1} (X - U_i) \qquad (6)$$

The discriminant $g_i(X)$ is calculated for each class and the class with the highest value is selected for the final classification map.

2.3.2. Surface Temperature

Retrieval of land surface temperature (LST) from ASTER TIR data requires decoupling surface temperature and emissivity. The standard TES algorithm developed for ASTER (Gillespie et al., 1998), adaptable also for other multispectral images, relies on an empirical relationship between spectral contrast and minimum emissivity to equalize the number of unknowns and measurements so that the set of Planck equations for the measured thermal radiance (L) can be inverted. The TES algorithm consists of four modules, i.e., normalized emissivity method (NEM), ratio (RAT), maximum-minimum difference (MMD) and quality assurance (QA). Briefly, the NEM algorithm estimates initial temperature (T) values, from which NEM emissivities are estimated. By rationing the NEM emissivities using the RAT module, relative emissivities (β) can be found. Subsequently, in the MMD module, the β spectrum is scaled to actual emissivity *(ε)*, and temperatures are recalculated. Finally, the QA module evaluates the accuracy of the product (T, *ε*). More details about the TES algorithm can be found in Gillespie (1998).

Generally, prior to the TES process, the following pre-processes must be applied to the ASTER TIR Level 3A data: radiance conversion, radiance recalibration and atmospheric correction. The radiance conversion is attained by means of unit conversion coefficients (UCC, Table 1) available from the header file. Radiance recalibration is not needed for the version 3 radiometric calibration coefficients (RCCs) employed in this study, since in 3.00 or later version RCC's have been determined using regression equations (Tonooka et al., 2004). Two atmospheric correction methods, standard atmospheric correction (Palluconi et al., 1999) and water-vapor scaling (WVS) method (Tonooka, 2001), are performed in this study. Brief explanations about both atmospheric corrections are given below.

Table 1. Central wavelength and conversion coefficient for TIR channels of the ASTER sensor.

Band	Central wavelength (μm)	Conversion coefficient (10^{-3})
10	8.30	6.822
11	8.65	6.780
12	9.10	6.590
13	10.6	5.693
14	11.3	5.225

2.3.3. Theoretical Basis of ASTER Standard Atmospheric Correction

The standard atmospheric correction algorithm is based on radiative transfer calculation using the MODTRAN code, which gives better results of TES as compare to LOWTRAN (Palluconi et al., 1999). MODTRAN code allows the retrieval of at-surface temperatures using atmospheric parameters estimated on a pixel-by-pixel basis. Major sources of atmospheric profiles and other MODTRAN data inputs used in ASTER/TIR atmospheric correction are the global data assimilation system (GDAS) product, provided by National Centers for Environmental Prediction (NCEP), and the Global 30 Arc Second Elevation Data Set (GTOPO30) interpolated to obtain surface elevation of each pixel. Other atmospheric profiles such as molecular scattering/ absorption are taken from models incorporated in the MODTRAN code. The radiation transfer calculation is implemented at each grid point of the ASTER/TIR image data.

The theoretical basis of radiative transfer for atmospheric correction in the TIR spectral region has been described in a previous paper (Tonooka and Palluconi, 2005). With the assumption that variation of spectral emissivity is small and sensor bandwidth is adequately narrow, the sensor radiance under clear sky conditions can be approximated as:

$$I_i = \tau_i(\theta)\left[\grave{o}_i B_i(T_s) + (1-\grave{o}_i)I_i^{\downarrow}\right] + I_i^{\uparrow}(\theta) \quad (7)$$

where i is the band number, θ is the view angle, $\grave{o}_i$ is the surface emissivity, T_s is the surface kinetic temperature, $B_i(T_s)$ is the Planck function, $T_i(\theta)$ is the atmospheric transmittance, $I_i^{\uparrow}(\theta)$ is the path radiance, and $I_i^{\downarrow}$ is the downward sky radiance.

By using the radiative transfer calculation combined with the atmospheric profile, at-surface radiance $I_{s,i}$ can be derived as

$$I_{s,i} \equiv \grave{o}_i B_i(T_s) + (1-\grave{o}_i)I_i^{\downarrow} = \frac{I_i(\theta) - I_i^{\uparrow}(\theta)}{\tau_i(\theta)} \quad (8)$$

The separation between $\grave{o}_i$ and T_s can be achieved by means of the following empirical equation (Gillespie et al., 1998):

$$\grave{o}_{min} = 0.994 - 0.68 \times MMD^{0.737} \quad (9)$$

where $\grave{o}_{min}$ is the minimum emissivity and MMD is the maximum-minimum difference of apparent emissivity.

The standard atmospheric correction algorithm performs well in dry conditions, but less well under humid conditions. The water vapor scaling (WVS) method (Tonooka, 2001), on the other hand, has proven to perform better in humid area as compared to the standard algorithm. Since the study area is located in tropical area and the mud stream erupted in high temperature, the WVS algorithm will be considered in this study and a brief description of the method is given below.

2.3.4. Theoretical Basis of Atmospheric Correction Using WVS Method

The WVS method is a combination of the standard atmospheric algorithm and an extended version of differential absorption algorithm, which is known as the extended multichannel/ water-vapor-dependent (EMC/WVD) algorithm. Originally, this algorithm was not proposed for the atmospheric correction of ASTER/TIR (Pallucconi et al., 1999) for the following three reasons: first, ASTER/TIR channels are located in the clearest atmospheric window region; second, the emissivity of land surface is generally not known as it is on water; and third, the algorithms are very sensitive to the measurement noise inherent in the instrument. Nevertheless, the EMC/WVD algorithm can be employed to improve atmospheric profiles used as input data to MODTRAN. Theoretically, the EMC/WVD algorithm is expressed as

$$\begin{cases} T_{g,i} = \alpha_{i0} + \sum_{k=1}^{n} \alpha_{ik} T_k \\ \alpha_{ik} = p_{ik} + q_{ik}W + r_{ik}W^2 (k = 0, 1, \ldots, n) \end{cases} \quad (10)$$

where i is the band number, n is the number of bands, W is the estimated the total water-vapor amount (g/cm^2), p, q, r are the regression coefficient for each band and T_k is the brightness temperature measured by band k (K), and $T_{g,i}$ is the at-surface brightness temperature for band i, defined by

$$T_{g,i} = B_i^{-1}\left(I_{s,i}\right) \quad (11)$$

Here B_i^{-1} is the inverse Planck Function. For better accuracy, the algorithm is applied only to "gray" pixels (covered by materials with nearly constant emissivity close to unity), such as water, vegetation and some types of soil.

On the other hand, the algorithm should find an appropriate water-vapor scaling factor γ to improve the water-vapor profiles of globally assimilated data. The parameter γ is defined by

$$\gamma = \frac{U'}{U} = \frac{w'(h)}{w(h)} \quad (12)$$

where U and U' are total water-vapor amounts for the original and scaled profile, respectively, and $w(h)$ and $w'(h)$ are the corresponding water-vapor amounts at height h. Assuming that τ_i can be expressed by the Pierluissi double-exponential band model formulation (Tonooka, 2005), the scaling factor γ can be calculated for each gray pixel using $T_{g,i}$ given by the EMC/WVD algorithm. The TIR multispectral data are atmospherically corrected using WVD methods by applying the following processes successively: selecting gray pixels from the image, estimating the value of water scaling factor γ of each gray pixel by using the EMC/WVD method, estimating the γ value of non-gray pixels by means of horizontal interpolation, improving the water-vapor profiles of global assimilated data with γ values, calculating the atmospheric parameters with the improved profiles, and correcting the measured radiances atmospherically.

In the actual application of the WVS method to ASTER/TIR data, further improvements have been made regarding the introduction of band-dependent γ as well as the gray pixel selection (Tonooka, 2005).

3. Results and Discussion

Figures 2 (a-c) show the false color composite (FCC) of ASTER VNIR images (R: band 3N, G: band 2 and B: band 1) before (3 November 2005) and after the mud eruption (3 September 2006 and 13 November 2006). Figures 2 (d-f) show

corresponding images overlaid with NDVI distributions (gray color indicates NDVI values between -0.5 and 0).

The gray color in Figure 2 (d-f) shows non-vegetation areas (including hot mud, mixed with other objects), since reflectance in those areas is stronger in red channel rather than in infrared channel (Hot mud flow website, 2007). In the figure, it is obvious that the vegetation (paddy field and crop field) coverage has reduced after the mud eruption.

Since the NDVI distribution is not sufficient for the accurate determination of mud area size, here we apply the supervised, maximum likelihood classification to the ASTER VNIR images. Figures 2 (g-i) show the classification results which before (3 November 2005) and after (3 September and 13 November 2006) the mud eruption. Four classes that appear in the image before the eruption are vegetation (green), residence (yellow), water (blue) and road (white), whereas this last category (road) is replaced by mud (gray) in images after the eruption. Figures 2 (j) and (k) show FCC images of ASTER VNIR overlaid with the mud area class.
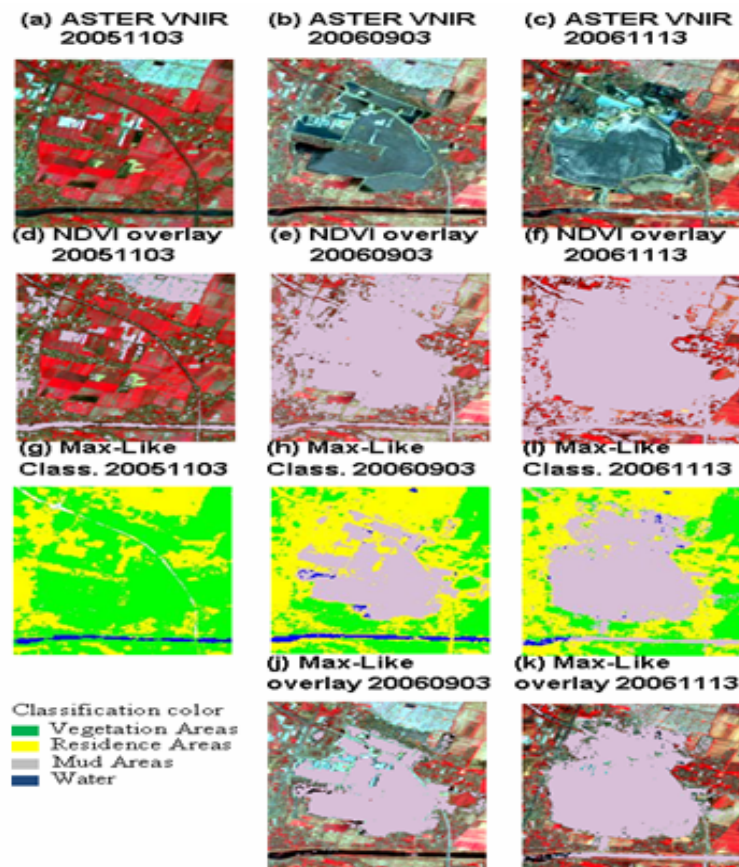

Figure 2. (a-c)False color composite (FFC, R:Band 3N,G:B2,B:B1) of all observation data, (d-f) NDVI with the value from -0.5 to 0, overlaid on the FCC image, gray color indicates non-vegetation areas (g-i) maximum likelihood classification of all data, (j-k) mud areas of maximum classification overlaid on the FCC image. Gray color indicates mud areas.

Table 2. Confusion matrix, overall accuracy and kappa coefficient of maximum likelihood classification.

Confusion matrix for 20051103

	Vegetation	Residence	Water	Road
Vegetation	1451	65	1	0
Residence	28	432	0	0
Water	0	0	100	0
Road	12	0	0	50

Confusion matrix for 20060903

	Vegetation	Residence	Water	Mud
Vegetation	1059	77	0	0
Residence	28	1023	2	20
Water	0	0	170	5
Mud	0	41	0	955

Confusion matrix for 20061113

	Vegetation	Residence	Water	Mud
Vegetation	810	76	0	40
Residence	39	1694	0	153
Water	0	0	64	5
Mud	32	86	1	2020

Overall Accuracy and Kappa Coefficient

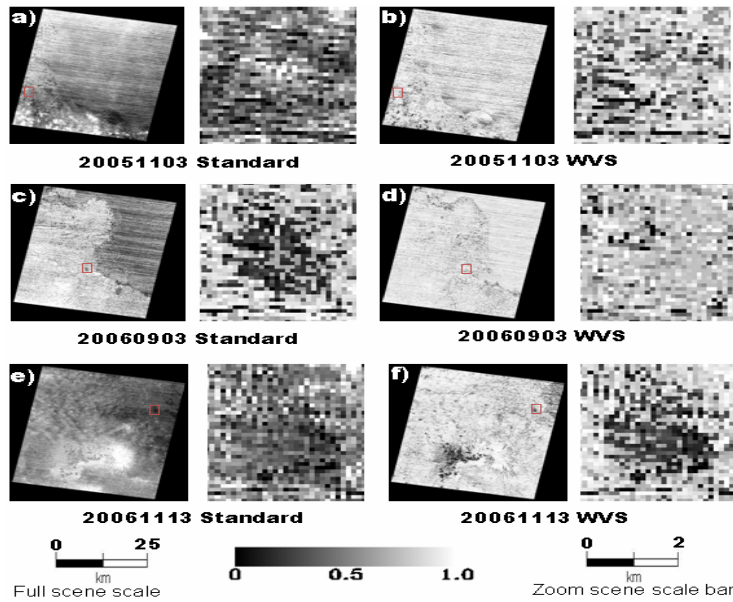|	20051103	20060903	20061113
Overall Acc. (%)	95.0	94.8	91.4
Kappa Coeff.	0.89	0.93	0.86

Figure 3. Emissivity map of band 11 from each observation data. Panels a, c and e are from atmospheric correction using the standard method. Panels b, d, and f are from that using Water Vapor Scale Method. Right side images are zoom images of red rectangles shown in left side panels.

Classification result on 3 September 2009 shows that the mud has spread to the southern part of drilling well. Residence classes are still seen in the middle of mud area since this residence area has not sunk below the mud surface. Similarly the roof of the factory can also be distinguished clearly in Figure 2 (b). The water classes indicate the Porong River and the boundary of embankment, since in this area mud particles have settled below the water level. On 13 November 2009, the mud area increased drastically with the disappearance of the residence area. The mud diverted to the Porong River is also correctly classified.

Although some misclassifications still occur, the maximum-likelihood classification yields better detection of mud areas than that based on NDVI. Table 2 shows the confusion matrics, overall accuracies, and kappa coefficients for all the data. The confusion matrix contains information about statistics for assessing image classification accuracy by showing the degree of misclassification among classes (Provost and Kohavi, 1998) and the kappa coefficient shows the statistical measure of the agreement. The overall accuracies are estimated to be 95.0%, 94.8%, and 91.4% for data on 3 November 2005, 3 September 2006, and 13 November 2006, respectively.

Figures 3 and 4 show the distributions of emissivity and surface temperature, respectively, comparing the results between the standard and WVS methods of atmospheric correction. In the emissivity maps derived from band 11 (Figure 3), similar distributions are found for the two methods on each observation day, but the WVS method yields better emissivity on the sea surface area (Figure 3 (b) and (d)) as compared with the standard method (Figure 3 (a) and (c)). The WVS results exhibit homogeneous and almost unity emissivity over the sea surface area, as expected. Also, the WVS method shows better cloud detection and gives lower emissivity value for areas covered by cloud, shown on the lower part of Figure 3 (a-b) and (e-f). As summarized in Table 3, emissivity values derived with the WVS method are generally higher than those with the standard method. The results obtained with the WVS method show lower temperatures than those with the standard method due to the difference in emissivity mentioned above.

Table 3. Emissivity values after atmospheric correction using standard and WVS method for each observation date.

		Standard			WVS		
		Min	Max	Mean	Min	Max	Mean
3 Nov 2005	Band 10	0.00	0.99	0.80	0.47	1.00	0.96
	Band 11	0.00	0.99	0.84	0.82	1.00	0.97
	Band 12	0.00	0.99	0.87	0.78	1.00	0.97
	Band 13	0.00	1.00	0.93	0.75	1.00	0.98
	Band 14	0.00	0.99	0.95	0.75	1.00	0.97
3 Sept 2006	Band 10	0.78	1.00	0.94	0.81	1.00	0.98
	Band 11	0.82	1.00	0.95	0.84	1.00	0.98
	Band 12	0.85	1.00	0.96	0.84	1.00	0.98
	Band 13	0.82	1.00	0.97	0.82	1.00	0.98
	Band 14	0.78	1.00	0.97	0.79	1.00	0.98
13 Nov 2006	Band 10	0.56	0.99	0.88	0.64	1.00	0.97
	Band 11	0.73	1.00	0.91	0.81	1.00	0.97
	Band 12	0.79	1.00	0.92	0.84	1.00	0.97
	Band 13	0.83	1.00	0.95	0.82	1.00	0.97
	Band 14	0.75	1.00	0.96	0.78	1.00	0.97

Figure 4 shows surface temperature distributions retrieved inside and outside the embankment. The black or white line in each panel shows the location of embankment line during the observation time (for the sake of comparison, the area is also indicated for panels before eruption). The three surface temperature images indicate that the temperature difference between the inside and outside of the embankment was not large. The water content of the mud has possible contribution to this result. Since the water content will raise the heat capacity and give the latent heat flux, the mud temperature was less sensitive to sun radiation and air temperature changes in comparison to surrounding areas, thus resulting in small temperature differences between the inside and outside of the embankment.

Applying current methodology in nighttime images (without sun radiation effect) in the future study is estimated will give better result for visualizing such kind of disaster. Surface temperature distributions outside the embankment from three different observation times show similar patterns, though on 3 September 2006, the temperature decreased both outside and inside the embankment (Table 4) as compared to other observations. The surface temperature data taken at the nearest observation station to the study area (Surabaya/Juanda) also indicate that the air temperature was lower at the beginning of September 2006 (including 3 September 2006), by 5-6°C compared to 3 November 2005 and 13 November 2006 (Figure 5). Data on Figure 5 were retrieved from global surface summary of the day (GSOD), one product of National Climate Data Center (National Climate Data Center (NCDC), 2006).
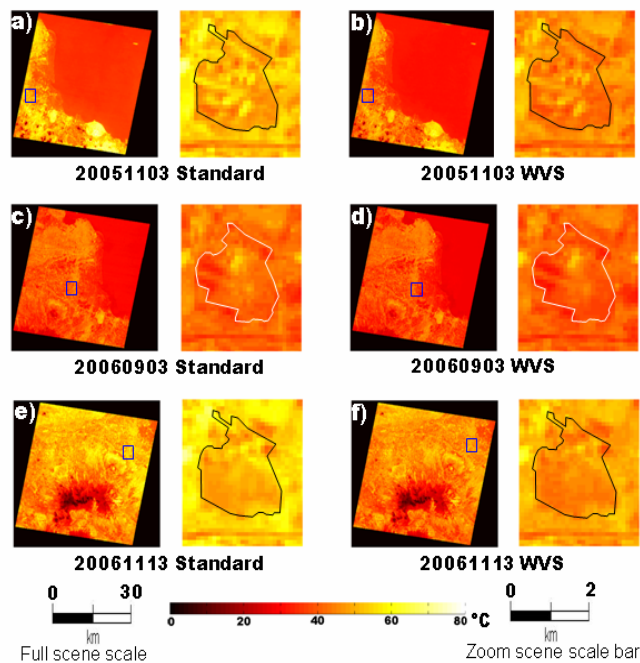

Figure 4. Surface temperature of mud eruption site, retrieved after atmospheric correction by standard and WVS methods for each observation date. Right side images are zoom images of blue rectangles in left side panels.

Comparison of Figure 4 (b) and (d) indicates that the temperature inside the embankment is lower after the mud eruption (30.5-53.4°C on 3 September 2006) than before the mud eruption (36.7-55.9°C on 3 November 2005). This is also related the lower air temperature, in addition to the mud composition with high water content on 3 September 2006. A close examination, however, shows that some parts inside the embankment, including the center of the eruption, exhibit higher temperatures than remaining parts.

In relation to Figure 2 (a), high temperatures in Figure 4 (b) and (d) are detected also over residence, road covered with asphalt, bare land and dry bare land (non red-color parts in Figure 2 (a)), presumably causing relatively strong reflection of sunlight during the ASTER observation time (10.30 at local time). In the center left area of Figure 2 (b), sedimentation of the mud resulted in the appearance of water surface inside the embankment. The corresponding areas in Figure 4 (c-d) indeed show lower temperatures. On 13 November 2009, the center of eruption exhibits higher temperature compared to other parts. Relatively high temperature observed at the bottom right part of the observed area is due to dry bare land, which was covered with mud on 3 September 2009. Thus, temperature on this part increased during the period between the two observations. Table 4 shows the statistics of the retrieved surface temperature.

Since the area of mud spread is mostly delineated by the embankment position, the visual interpretation of the ASTER VNIR data, with the help of news information (Hot mud flow website, 2007) can be used to estimate the hot mud spreading area on a particular date. This method leads to the estimations of $(2.6\pm0.1)\times10^6$ m^2 and $(2.9\pm0.1)\times10^6$ m^2

for areas on 3 September 2006 and 13 November 2006, respectively.

Although digital elevation model (DEM) data from stereo vision are included in the ASTER level 3A data, the height of the embankment cannot be retrieved because of DEM errors. The errors are ascribed to the fact (Watanabe, 2005), that the matching process sometimes does not work well in homogenous areas such as sea or lake. Moreover, since the DEM retrieval algorithm relies on fixed size windows for matching (i.e. calculation of spatial correlation), slopes appear smoother than their actual situations. Thus, instead of DEM analysis, here we make an assumption that height of the embankment is 15 ± 4 m to estimate the volume of mud. This estimation is based on our ground survey conducted on 8 November 2006. As a result, the mud volumes on 03 September 2006 and 13 November 2006 are estimated to be $(3.8\pm1.0)\times10^7$ m^3 and $(4.3\pm1.2)\times10^7$ m^3, respectively. From the mud sample taken during the ground survey, the density of mud and water mixture is (1.4 ± 0.2) g/cm^3. Therefore, the total weight of the mud is calculated to be $(5.4\pm2.0)\times10^{10}$ kg and $(6.1\pm2.3)\times10^{10}$ kg, respectively.
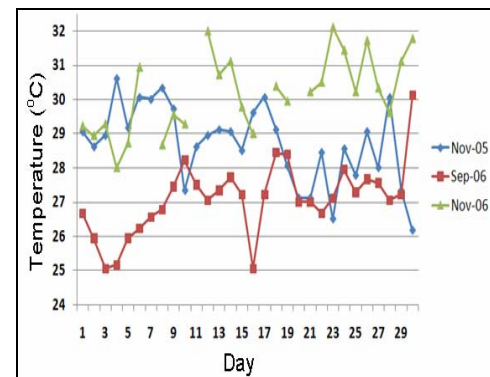

Figure 5. Daily mean air temperature observed at Surabaya/Juanda station in November 2005, September 2006 and November 2006.

Table 4. Surface temperature on the mud eruption site after atmospheric correction
using standard and WVS method for each observation date.

	3 Nov 2005			3 Sep 2006			13 Nov 2006		
	Min	Max	Mean	Min	Max	Mean	Min	Max	Mean
Standard (^{o}C)	40.7	61.9	49.9	32.5	55.1	41.3	41.1	68.3	50.8
WVS (^{o}C)	36.7	55.9	44.1	30.5	53.4	39.2	37.9	60.4	45.9

4. Summary

In this research we have investigated the regional effect of the hot mud eruption in east Java using the ASTER imagery. The VNIR data are used to delineate the mud area, and the TIR data are used for the estimation of surface temperature. Classifications based on NDVI and maximum-likelihood methods have been tested for extracting the mud spreading area from VNIR data. While the NDVI method is useful to detect changes in vegetated areas, better accuracy is obtained with the supervised, maximum-likelihood classification method in terms of the retrieval of mud spreading area.

Surface temperature was retrieved from the ASTER TIR data using the standard TES algorithm. Prior to the TES, both the standard and WVS atmospheric correction algorithms have been applied and compared. It was turned out that the WVS method performs better for humid area than the standard method, giving uniform and almost unity emissivity values on sea surface areas, as expected.

The information retrieved on hot mud eruption can be summarized as follow. The mud area was $(2.89\pm0.10)\times106$ m^2 and the temperature of the mud, retrieved with the WVS method, was 37.8 to 60.4°C on 13 November 2006. Assuming the mud depth of 15 ± 4 m, mud volume and weight on 13 November 2006 were estimated as $(4.3\pm1.2)\times107$ m^3 and $(6.1\pm2.3)\times1010$ kg, respectively. As a whole, this research has demonstrated the capability of the ASTER data product in offering regional estimation of the parameters that are indispensable for evaluating and confronting a large scale calamity.

5. References

Abrams, M., 2000, The Advanced Spaceborne Thermal Emission and Reflection Radiometer (ASTER): Data products for the high spatial resolution imager on NASA's Terra platform. *International Journal of Remote Sensing*, 21:847-859.

BAKOSURTANAL, 1997. Sheet 1608-134 Porong, Badan Koordinasi Survey dan Pemetaan Nasional, Bogor, Indonesia.

Berthier, E., Y. Arnaud, R. Kumar, S. Ahmad, P. Wagnon, and P. Chevallier, 2007, Remote sensing estimates of glacier mass balances in the Himachal Pradesh (Western Himalaya, India). *Remote Sensing of Environment*, 108:327-338.

Brack, C. L., 2007, National forest inventories and biodiversity monitoring in Australia. *Plant Biosystems*, 141:104-112.

Cyranoski, D., 2007, Indonesian eruption: Muddy waters. *Nature*, 445:812-815.

Davies, R. J., R. E. Swarbrick, R. J. Evans, and M. Huuse, 2006, Birth of a mud volcano: East Java, 29 May 2006. *GSA Today*, 17:4-9.

Fujisada, H., 1994, Overview of ASTER instrument on EOS-AM1 platform. In Proc. SPIE, pp. 14-36.

Gillespie, A., S. Rokugawa, T. Matsunaga, J. S. Cothern, S., Hook, and A. B. Kahle, 1998, A temperature and emissivity separation algorithm for

Advanced Spaceborne Thermal Emission and Reflection Radiometer (ASTER) images. IEEE *Transactions on Geoscience and Remote Sensing*, 36:1113-1126.

Hot mud flow website, 2007, Hot mud flow in east java, Indonesia website, Retrieved 19 June 2007, from http://hotmudflow.wordpress.com/.

Hussin, Y. A. and V. P. Atmopawiro, 2004, Sub-pixel and maximum likelihood classification of landsat ETM+ images for detecting illegal logging and mapping tropical rain forest cover types in berau, east Kalimantan, Indonesia. *International Society for Photogrammetry and Remote Sensing*, 35:933-944.

Mazzini, A., H. Svensen, G. G. Akhmanov, G. Aloisi, S. Planke, A. Malthe-Sørenssen, and B. Istadi, 2007, Triggering and dynamic evolution of the LUSI mud volcano, Indonesia. *Earth and Planetary Science Letters*, 261:375-388.

McRoberts, R. E. and E. O. Tomppo, 2007, Remote sensing support for national forest inventories. *Remote Sensing of Environment*, 110:412-419.

Mezned, N., S. Abdeljaoued, and M. R. Boussema, 2007. ASTER Multispectral Imagery for Spectral Unmixing based Mine Tailing Cartography in the North of Tunisia. *in* Conference of the Remote Sensing & Photogrammetry Society Newcastle.

Miura, T., H. Yoshioka, K. Fujiwara, and H. Yamamoto, 2008, Inter-comparison of ASTER and MODIS surface reflectance and vegetation index products for synergistic applications to natural resource monitoring. *Sensors*, 8:2480-2499.

Muukkonen, P. and J. Heiskanen, 2007, Biomass estimation over a large area based on standwise forest inventory

data and ASTER and MODIS satellite data: A possibility to verify carbon inventories. *Remote Sensing of Environment*, 107:617-624.

National Climate Data Center (NCDC), 2006, Global Summary of the Day (GSOD), Retrieved 14 November 2009, from http://www7.ncdc.noaa.gov/CDO/cdoselect.cmd?datasetabbv=GSOD&countryabbv=&georegionabbv=.

Normile, D., 2006. Mud Eruption Threatens Villagers in Java. *Science*, pp. 1865.

Palluconi, F., G. Hoover, R. Alley, M. Jentoft-Nilsen, and T. Thompson, 1999. An atmospheric correction method for ASTER thermal radiometry over land, ASTER algorithm theoretical basis document (ATBD), Revision 3, Jet Propulsion Lab, Pasadena, CA.

Paola, J. D. and R. A. Schowengerdt, 1995, A detailed comparison of backpropagation neural network and maximum-likelihood classifiers for urban land use classification. *IEEE Transactions on Geoscience and Remote Sensing*, 33:981-996.

Paul, F., C. Huggel, and A. Kääb, 2004, Combining satellite multispectral image data and a digital elevation model for mapping debris-covered glaciers. *Remote Sensing of Environment*, 89:510-518.

Pieri, D. and M. Abrams, 2004, ASTER watches the world's volcanoes: a new paradigm for volcanological observations from orbit. *Journal of Volcanology and Geothermal Research*, 135:13-28.

Provost, F. and R. Kohavi, 1998, Guest Editors Introduction: On Applied Research in Machine Learning. *Machine Learning*, 30:127-132.

Pu, R., P. Gong, R. Michishita, and T. Sasagawa, 2006, Assessment of multi-

resolution and multi-sensor data for urban surface temperature retrieval. *Remote Sensing of Environment*, 104:211-225.

Public Work Department Website, 2008, Rain fall data, Retrieved 20 July 2008, from www.dpuairjatim.org/data/ download/Data%20Hujan.pdf.

Ramsey, M. and J. Dehn, 2004, Spaceborne observations of the 2000 Bezymianny, Kamchatka eruption: The integration of high-resolution ASTER data into near real-time monitoring using AVHRR. *Journal of Volcanology and Geothermal Research,* 135:127-146.

Sidoarjo District Website, 2006, Selayang pandang kabupaten Sidoarjo, Retrieved 20 January 2007, from http://www. sidoarjokab.go.id/selayang/01_info_um um.php.

Surabaya Goverment Website, 2006, Geografi kota Surabaya, Retrieved 5 February 2007, from http://www. surabaya.go.id/geografis.php.

Tonooka, H., 2001, An atmospheric correction algorithm for thermal infrared multispectral data over land-a water-vapor scaling method. *IEEE Transactions on Geoscience and Remote Sensing*, 39:682-692.

Tonooka, H., 2005, Accurate atmospheric correction of ASTER thermal infrared imagery using the WVS method. *IEEE*

Transactions on Geoscience and Remote Sensing, 43:2778-2792.

Tonooka, H. and F. D. Palluconi, 2005, Validation of ASTER/TIR standard atmospheric correction using water surfaces. *IEEE Transactions on Geoscience and Remote Sensing*, 43:2769-2777.

Tonooka, H., F. Sakuma, M. Kudoh, and K. Iwafune, 2004. ASTER/TIR onboard calibration status and user-based recalibration. in Proceeding SPIE, pp. 191-201, *eds.* Roland, M., P. Steven, N., S. Haruhisa, B. L. Joan, and L. A. Michelle. SPIE.

Tralli, D. M., R. G. Blom, V. Zlotnicki, A. Donnellan, and D. L. Evans, 2005, Satellite remote sensing of earthquake, volcano, flood, landslide and coastal inundation hazards. ISPRS *Journal of Photogrammetry and Remote Sensing*, 59:185-198.

Tucker, C. J., 1979, Red and photographic infrared linear combinations for monitoring vegetation. *Remote Sensing of Environment,* 8:127-150.

UNDAC, 2006. Environmental Assessment hot mud flow East Java, Indonesia, United Nation Disaster Assessment and Coordination (UNDAC), Geneva, Switzeland.

Watanabe, H., 2005, Accuracy of geolocation and DEM for ASTER. *Proceeding of ISPRS*, 5978:21-30.